Available online at www.sciencedirect.com

jmr&t Journal of Materials Research and Technology

journal homepage: www.elsevier.com/locate/jmrt

Investigation of the applicability of Cu–Fe–Mn–Ni based high entropy and compositionally complex alloys as metal matrix composites for cobalt free hot-pressed diamond tools

Christian Timmer[*], *Wolfgang Tillmann*, *Lukas Wojarski*, *Manuel Pinho Ferreira*

Institute of Materials Engineering (LWT), Technical University of Dortmund, 44227 Dortmund, Germany

ARTICLE INFO

Article history:
Received 29 May 2023
Accepted 28 August 2023
Available online 29 August 2023

Keywords:
CALPHAD simulation
Mechanical alloying
High-entropy alloys (HEAs)
Compositionally complex alloys (CCAs)
Hot pressing
Diamond tools

ABSTRACT

Due to the rising demand and carcinogenic effect of cobalt, alternative metal matrixes need to be developed for hot-pressed diamond tools. Due to this reason High-Entropy alloys without cobalt were calculated via phase fraction diagrams. Three alloys of the Al–Cu–Fe–Mn–Ni system Al30Cu30Fe5Mn25Ni10, Al11.25Cu35Fe5Mn20Ni28.75 and Al5Cu20-Fe25Mn25Ni25 were chosen due to their different crystal structures ranging from pure bcc, eutectic fcc-bcc to pure fcc crystal structure. Cr5Cu20Fe25Mn25Ni25 was chosen to verify the change of one element on the consolidation properties. The alloys were mechanically alloyed and hot-pressed at 800 °C for 3 min without and at 900 °C for 3 min with diamonds. Porosity increased with the fraction of bcc solid solution in the investigated alloys of the Al–Cu–Fe–Mn–Ni system. Samples consisting of Cr5Cu20Fe25Mn25Ni25 showed the lowest porosity, which was attributed to precipitation of a second copper-rich fcc solid solution around the remaining pores. At a process temperature of 800 °C and 3 min isothermal hold the samples featured a porosity of only 2.72%. Within the XRD patterns and SEM images of the hot-pressed samples with diamonds no graphitization or formation of carbides could be observed. Therefore, Cr5Cu20Fe25Mn25Ni25 was identified as a promising cobalt free metal-matrix candidate for diamond tools.

1. Introduction

High-entropy alloys (HEA) are a new alloying concept developed by two different research groups in the year 2004. Cantor et al. melted two alloys containing 16 and 20 elements respectively. In both alloys a single face-centered cubic (fcc) structure with equimolar ratios of Co, Cr, Fe, Mn and Ni were identified [1]. Yeh et al. used a theoretical approach to HEAs. They explained their findings with Boltzmann's hypothesis on the interaction between entropy and the complexity of the alloys constitution to reduce the possibility of intermetallic phases. The configurational entropy rises logarithmically with the number of elements in equimolar or near equimolar ratio. Alloys with different amounts of equimolar transition metals were cast with face-centered cubic, body-centered cubic

* Corresponding author.
E-mail address: Christian.Timmer@tu-dortmund.de (C. Timmer).
https://doi.org/10.1016/j.jmrt.2023.08.272

structure or a mix of both. But no intermetallic phases were developed in any of the cast alloys. This confirms the hypothesis, that a higher entropy stabilizes solid solutions [2]. Due to the point that HEA are relatively new, there is no uniform definition. In this publication the definition by the German Research Foundation (DFG) of the priority program „Compositionally Complex Alloys - High Entropy Alloys (CCA-HEA)" (SPP 2006) is utilized. HEAs are defined as an alloy with at least 5 elements with an atomic fraction between 5% and 35% randomly occupying the sites of one crystal structure. While CCA are defined in the same compositional range with more than one crystal structure. HEA and CCA show superior properties in different fields depending on the crystal structure and elements used. The variation of the Al content of the $Al_xCoCrCuFeNi$ alloy led to a transition from a fully fcc HEA to a bcc crystal structure with a mix of both in between. The hardness increased from 200 HV to 600 HV [3]. The temperature dependent hardness loss is less in face centered cubic HEAs. The hardness value of the fcc-HEA $Al_{0,3}CoCrFeNi$ was reduced from 300 HV at room temperature to 190 HV at 1000 °C [4]. Additionally, by optimizing the compositional design of the alloys high wear resistance [5,6], high temperature oxidation [7] and high corrosion resistance [8] can be achieved. Due to these properties HEAs are a promising candidate as metal matrix for diamond metal matrix composites (MMC). Diamond MMCs are used for machining hard construction materials like granite basalt or concrete [9]. These are manufactured via powder metallurgical methods as grinding segments which are joined via brazing or laser welding to core drills, buzz, wire or gang saws [10,11]. For a long period of time, cobalt dominated as the metal part for diamond MMCs [12] but due to high fluctuations in the price of raw cobalt [13] and the identification of the that cobalt powder has a carcinogenic effect in mammals [14] the demand for alternatives arose. Therefore, blended powders with reduced or no cobalt content are frequently used [15]. The mechanical properties of the used pure metals and blended powders are significantly lower to those of the diamond grains which limits the performance capability of diamond tools [16]. Due to this point the current research focuses on the usage of pre-alloyed powders as metal matrix for diamond MMCs with a base of iron or copper to increase the mechanical and wear [17–19]. Non-metallic elements like phosphorous are also used to reduce the sintering temperature. These non-metallic melting point depressants tend to form brittle intermetallic phases reducing the ductility of the metal matrix [20]. Elements like manganese and tin are also used to reduce the sintering temperature. These pre alloyed powders show a significant rise in hardness compared to pure cobalt from 107 HV [21] to 352 HV [22].

While mechanical alloying and consolidation via hot pressing or spark-plasma sintering (SPS) is common processing route for HEAs [23–25] only two research groups investigated these as metal matrixes for diamond tools. Zhang et al. [26–28] and Peng et al. [29] investigated the alloy CoCrFeNi with the addition of Mo. They investigated the alloy $Co_{24.1}Cr_{24.1}Fe_{24.1}Ni_{24.1}Mo_{3.6}$ which does not match the above-mentioned definition of a HEA, but it is the only alloy investigated for the application in diamond tools which is close to the HEA composition. SPS was utilized to manufacture the diamond segments. A relative density of 98,8% was achieved at 1100 °C with 40 MPa pressure in vacuum. The alloy had only one fcc solid solution with a hardness varying between 460 HV and 520 HV [26]. SPS experiments with diamonds showed that at a sintering temperature below 900 °C the regular shape of the diamonds could be maintained. At 950 °C amorphous carbon phases and complex structures at nanoscale formed. At 1000 °C the diamond was reduced to half its initial size and chromium carbides formed in the interlayer [27]. Coating the diamonds with nickel and titanium prevented its degradation at 950 °C and increased the hardness of the metal matrix from 342 HV to 370 HV [28]. Peng et al. used vacuum hot pressing at 1200 °C with 15 MPa for 60 min to create diamond segments. A relative density of 94.5% could be achieved. The high sintering temperature led to an interaction with the graphite punch and die which caused the massive formation of molybdenum and chromium carbides [29]. The investigated alloy $Co_{24.1}Cr_{24.1}Fe_{24.1}Ni_{24.1}Mo_{3.6}$ is not that well suited as an alloy for diamond tools due to the high sintering temperature and the degradation of the diamonds. Additionally, the alloy includes cobalt.

Concluding the state of the art, HEA and CCA are very promising metal matrixes for diamond MMCs. The high entropy of these alloys enables the combination of elements in higher amounts which would normally create intermetallic phases. Additionally, the number of possible alloys due to the possible element combinations enables alloys without cobalt. But the main point is the increase mechanical properties which depend highly on the resulting crystal structure of the one or more solid solutions. Due to these points four HEA and CCA based on the Cu–Fe–Mn–Ni system were developed by CALPHAD calculations with Thermo-Calc to identify the influence of a fcc, bcc and both crystal structures depending on the constitution. The four alloys based on the Cu–Fe–Mn–Ni system used in this paper were chosen due to their high-temperature crystal structure in their phase fraction diagrams. These alloys were synthesized by mechanical alloying out of pure metal powders. Crystal structure (XRD) and melting range (DTA) were analysed and compared to the simulation results. The alloys were hot pressed and the crystal structure (XRD), chemical composition (EDS), hardness and porosity were identified. The consolidation experiments were done at 800 °C to identify the influence of the crystal structure on the consolidation properties and at 900 °C to provoke a reaction between the diamonds and the carbide forming and catalytic acting elements.

2. Materials and methods

The thermodynamic simulations were performed with Thermo-Calc 2017a [30] and the TCHEA2 [31,32] database. To investigate the broad constitutional range of HEAs a script was written in order to generate numerous phase fraction diagrams. Per iteration the atomic fraction of one particular element was decreased by 5% while it was increased for another element. The whole script contained 513 different combinations with the thresholds of A20B20C20D20E20 and A35B35C20D5E5, where A-E are different elements, and the number represents the atomic percentage of the element. Al, Cr, Cu, Fe, Mn, Ni, Si and Ti were chosen as elements in the simulation.

To investigate the chosen alloys experimentally, elemental powders are needed for the mechanical alloying process. In

Table 1 the contaminations and the particle sizes of the used elemental powders are noted.

The ball mill used in this research was a Fritsch GmbH Pulverisette 5/4 with four 500 ml hardened chromium steel vials. 10 mm hardened chromium steel balls were used. 50 g of the blended powder mixture and 400 g of steel balls were put into each vial, resulting in a ball to powder ratio of 8:1. Additionally, stearic acid was added as a process control agent with an amount of 2 wt.% of the metal powder. The vials were filled up to 25 vol.-% in total. Argon was utilized to prevent oxidization during the alloying process. As milling parameters 300 rpm were used for 24 h. These parameters are based on the experience and were verified by different research groups using these parameters for synthesizing HEA via mechanical alloying [33,34].

The mechanically alloyed materials were consolidated by an CSP100 hot press (Dr. Fritsch GmbH). A punch and die system made of graphite was used to produce the samples. In every process four samples with a diameter of 15 mm were manufactured. 5 g of the different alloys were used per sample. The graphite dies and punches were coated with a boron nitride spray to prevent a mutual reaction and fusing with the graphite. During the whole process a constant pressure of 37 MPa was maintained on every sample. A constant flow of argon with 1000 l/h was utilized to protect the samples from excessive oxidization. Due to the unknown influence of the varying crystal structure of the HEA and CCA, a hot-pressing temperature of 800 °C was used to identify the consolidation properties. This was done to ensure a measurable porosity via light microscopy to identify the clear differences between the alloys and to gain insight on the consolidation properties. The holding time for every process were 3 min in accordance with industrial standard processes. After adding the diamonds, the temperature was raised to 900 °C to provoke reactions between the carbide forming and catalytic parts of the metal matrix alloys and the diamonds. The heating time was fixed on 10 min for every process. The samples were removed from the punch and die once the temperature dropped below 200 °C which was achieved after 30 min. 10 vol.-% of SDB1055 4050 mesh was added to the investigated alloys to create the diamond MMC samples.

The hardness of the consolidates HEA and CCA samples were performed after ISO 6507. The macro hardness was measured with HV10 and the micro hardness with HV0.1. Five measurements were taken for the macro and ten measurements for the micro hardness respectively.

To identify the melting ranges a Linseis STA PT 1600 differential thermal analysis system was utilized. The maximum temperature was set to 1400 °C with a heating rate of 10 K/min. In this process argon was also used as shielding gas.

Due to the lack of reliable data on the density of the chosen alloys, the Archimedes method to identify the relative density was not used in this research. Light microscopy was used instead to identify the porosity of the hot-presses samples. Ten optical micrographs were taken from each alloy and investigated by means of digital image analysis. The software takes advantage of the different contrast of the lighter consolidated samples and the darker pores.

Scanning electron microscopy (SEM) was performed using a field emission scanning electron microscope (JSM 7001F, Jeol GmbH) with secondary electron (ETD), backscattered electron (BSE) and energy dispersive x-ray (EDS) detectors.

Furthermore, X-ray diffraction was utilized to identify the crystal structure of the powders and the hot-pressed samples. Additionally, the interaction between the elements of the alloy with the diamonds were investigated in order to detected whether graphite and carbides have formed. The structural analysis was performed at the DELTA (Dortmund Electron Accelerator) Beamline 9 (BL9) [35]. A photon energy of 27 keV ($\lambda = 0.4592$ Å) was utilized with an MAR345 image plate detector with a beam size of 0.1 mm × 1 mm and an angle of 5°. The achieved data was integrated to a diffraction pattern via the FIT2D program [36]. To ensure comparability with other XRD measurements of HEA and CCA the 2-theta scale was converted to the wavelength of $\lambda = 1.5406$ Å. This wavelength equates with the Kα spectrum of a copper anode. The DELTA was used in other publications for the verification of graphitization or the formation of carbides between the metal matrix and diamonds in diamond MMCs [37–40].

3. Results and discussion

3.1. *Thermodynamic simulation*

The alloys were chosen based on the variation of the crystal structure and rather low melting points. Four alloys based on Cu–Mn–Fe–Ni with Al or Cr as the fifth element were chosen.

Table 1 – Chemical composition by the certificate of analysis of the elemental powders used for mechanical alloying.

Element (wt.%)	Al	Cr	Cu	Fe	Mn	Ni
Powder Provider	Alfa Aesar	Dr. Fritsch	Dr. Fritsch	Dr. Fritsch	Alfa Aesar	Dr. Fritsch
Particle size	<45 μm	<45 μm	<63 μm	<7 μm	<45 μm	<7 μm
Al	Bal.	–	–	–	–	–
C	–	0.02	–	0.04	–	0.1
Cr	–	Bal.	–	–	–	–
Cu	–	–	Bal.	–	–	–
Fe	0.105	0.2	–	Bal.	–	0.1
Mn	–	–	–	–	Bal.	–
N	–	0.02	–	0.01	–	0.005
Ni	–	–	–	–	–	Bal.
O	–	0.2	0.17	0.33	–	0.15
Undefined metal impurities	–	–	–	–	0.7	–

These alloys were Al30Cu30Fe5Mn25Ni10, Al5Cu20-Fe25Mn25Ni25, Al11.25Cu35Fe5Mn20Ni28.75 and Cr5Cu20-Fe25Mn25Ni25. The phase fraction diagrams of these alloys are shown in Fig. 1.

The three alloys of the Al–Cu–Fe–Mn–Ni system were chosen due to their varying high temperature crystal structure of pure bcc, eutectic fcc and bcc and pure fcc. These are Al30Cu30Fe5Mn25Ni10, Al11.25Cu35Fe5Mn20Ni28.75 and Al5Cu20Fe25Mn25Ni25 respectively. Additionally, Cr5Cu20-Fe25Mn25Ni25 was chosen due to the same high temperature crystal structure as Al5Cu20Fe25Mn25Ni25. A comparison between the consolidation properties of both alloys enables an insight of the influence of a single element on the sintering properties. Except for Al30Cu30Fe5Mn25Ni10 every alloy develops a second fcc phase between 600 °C and 800 °C. Additionally, the exchange of Al to Cr in Cr5Cu20Fe25Mn25Ni25 enables a sigma-phase to precipitate at around 800 °C while the CUB_A13 intermetallic phase precipitates below 650 °C in the Al30Cu30Fe5Mn25Ni10 alloy. Thermodynamic characteristics used by Yeh et al. to categorize HEAs and their crystal structure were calculated to verify the thermodynamic simulation with Thermo-Calc [41]. Every alloy used is close to the threshold of 1.5 times the ideal gas constant which was also introduced by Yeh, shown in Table 2. The enthalpy of mixing changed significantly due to the different elements and their amounts. Higher values of Al and reduced Fe contents increased the negative value of the mixing enthalpy in the Al–Cu–Fe–Mn–Ni system. The system changes with Cr instead of Al varied the enthalpy of mixing to positive values. Zhang et al. used the entropy of mixing and the atomic size difference to predict the microstructure of HEAs. The bulk of the fcc HEA analysed had slightly positive or negative enthalpies of mixing and an atomic size difference below 5%. With rising enthalpies of mixing and atomic size differences fcc-bcc dual phased alloys develop. Beyond a border of 6.6% in the atomic size difference intermetallic phases will form. The simulated high temperature crystal structure of the solid solutions is comparable with the data by Zhang et al. [42].

Table 2 – Calculated configurational entropy, enthalpy of mixing and atomic size difference calculated with equations from [43] with thermodynamic data from [44].

	ΔS_{Konf} [R]	ΔH_{mix} [kJ/mol]	δ [%]
Al30Cu30Fe5Mn25Ni10	1.45	−7.74	5.65
Al11.25Cu20Fe5Mn20Ni28.75	1.44	−3.28	4.29
Al5Cu20Fe25Mn25Ni25	1.51	−0.94	3.10
Cr5Cu20Fe25Mn25Ni25	1.51	1.88	1.17

3.2. *Mechanical alloying*

The particle size and melting range is significant in sintering processes. Lower particle sizes and melting ranges have a positive effect on the consolidation. In Table 3 the data for the

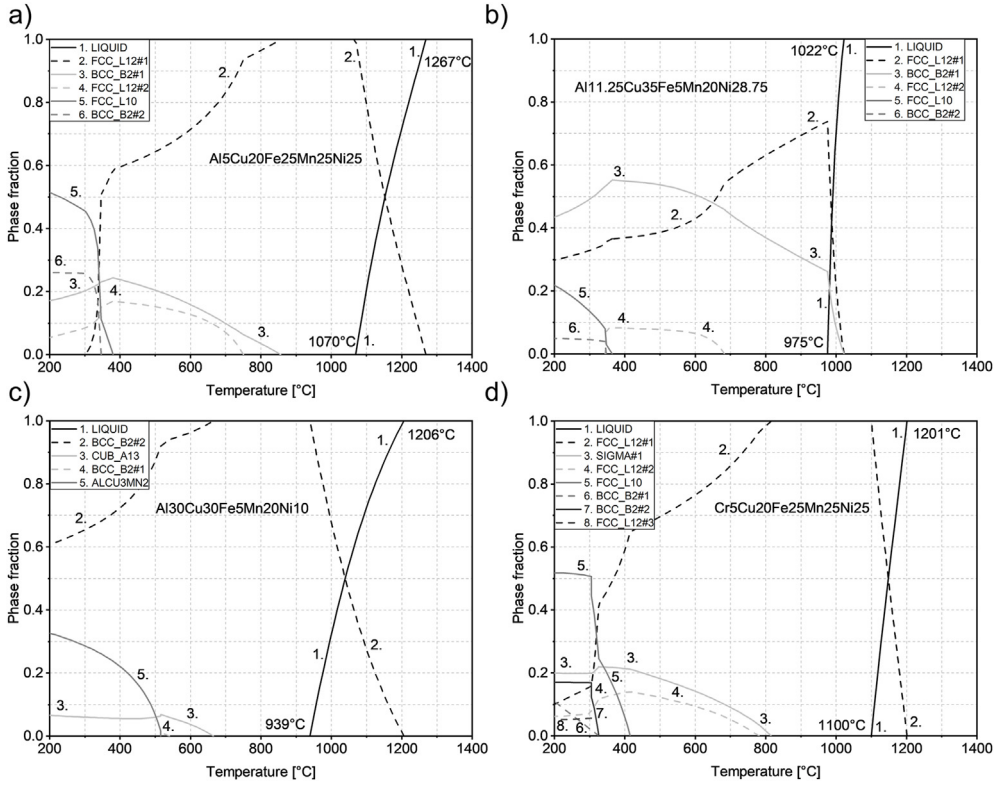

Fig. 1 – Phase fraction diagrams of the chosen alloys with a Cu–Fe–Mn–Ni base: a) Phase fraction diagram of Al30Cu30Fe5Mn25Ni10; b) Phase fraction diagram Al11.25Cu35Fe5Mn20Ni28.75; c) Phase fraction diagram of Al5Cu20Fe25Mn25Ni25 and d) Phase fraction diagram of Cr5Cu20Fe25Mn25Ni25.

Table 3 – Particle size and melting range of the mechanically alloyed powders.

	Particle size			Melting range			
				Simulation		DTA	
	d_{10}	d_{50}	d_{90}	T_L	T_S	T_L	T_S
Alloy	[μm]			[°C]			
Al30Cu30Fe5Mn25Ni10	0.38	0.52	1.14	1206	939	1142	988
Al11.25Cu20Fe5Mn20Ni28.75	3.97	6.32	11.91	1022	975	1070	1020
Al5Cu20Fe25Mn25Ni25	4.71	7.8	16.89	1267	1070	1287	1079
Cr5Cu20Fe25Mn25Ni25	3.76	6.23	13.44	1201	1100	1258	1051

chosen alloys is given. The fractions describe the percentage of particles with a size lower than the noted value. Al11.25Cu20Fe5Mn20Ni28.75, Al5Cu20Fe25Mn25Ni25 and Cr5Cu20Fe25Mn25Ni25 are with slight variations within the same size class. The particle size of the bcc HEA Al30Cu30-Fe5Mn25Ni10 is one magnitude lower than the rest of the mechanically alloyed particles. This is contributed to the higher hardness and lower cold working capabilities of bcc

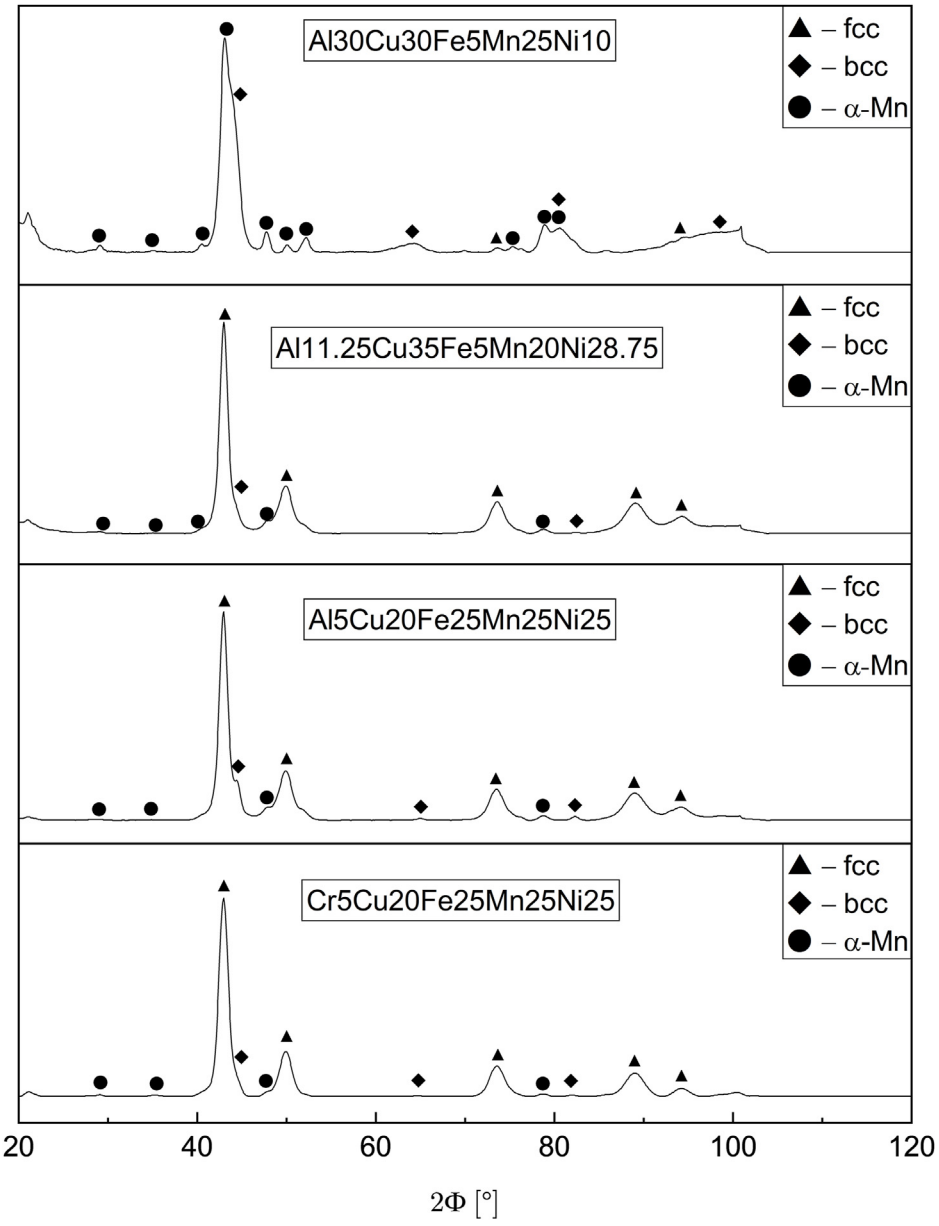

Fig. 2 – XRD patterns of the mechanically alloyed powders: a) Al30Cu30Fe5Mn25Ni10; b) Al11.25Cu35Fe5Mn20Ni28.75; c) Al5Cu20Fe25Mn25Ni25 and d) Cr5Cu20Fe25Mn25Ni25.

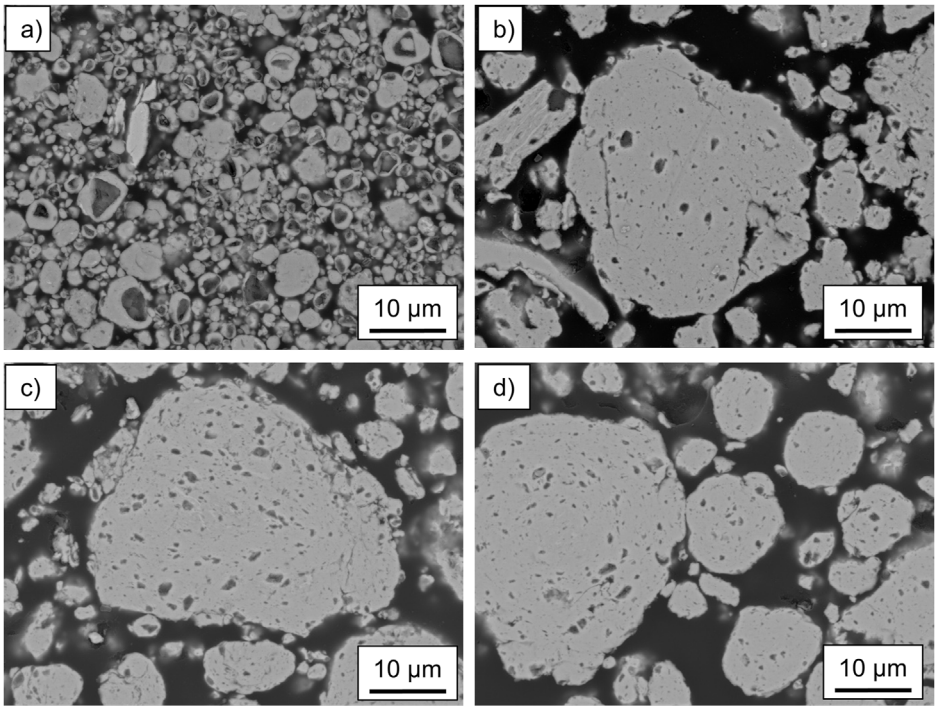

Fig. 3 – BSE images of cross sections including the mechanically alloyed powders: a) Al30Cu30Fe5Mn25Ni10; b) Al11.25Cu35Fe5Mn20Ni28.75; c) Al5Cu20Fe25Mn25Ni25 and d) Cr5Cu20Fe25Mn25Ni25.

HEAs. Additionally, it is the only alloy with a reduced liquidus temperature compared to the simulation. Overall, the liquidus and solidus temperature of the mechanically alloyed particles is about 50 °C higher then calculated by the phase fraction diagrams.

Fig. 2 shows the diffraction patterns of the mechanically alloyed powders. In exception of Al30Cu30Fe5Mn25Ni10 the peak with the highest intensity was determined to be a fcc crystal structure. Al11.25Cu20Fe5Mn20Ni28.75 and Al5Cu20Fe25Mn25Ni25 show additional peaks identified as a bcc and α-Mn crystal structure. While Al11.25Cu20Fe5Mn20Ni28.75 should crystallize with a fcc and bcc crystal structure as shown in the phase fraction diagram Al5Cu20Fe25Mn25Ni25 shows only a fcc structure at high temperatures. This indicates the point, that the bcc and α-Mn peaks were measured due to residue of unalloyed powders. Cr5Cu20Fe25Mn25Ni25 shows a less intense bcc and α-Mn peaks, which indicate a better homogenization in comparison with the alloys with Al content. Al30Cu30Fe5Mn25Ni10 on the other hand shows α-Mn as its highest peak and bcc as its secondary peak. In comparison to the other three alloys Al30Cu30Fe5Mn25Ni10 shows very broad peaks. This can be caused by smaller grain sizes in comparison to the other alloys. The main α-Mn and bcc peaks cannot be distinguished from each other. This indicates a very low grain size in these particles, which is typical for mechanically alloyed powders [45]. But overall, the existence of the bcc and α-Mn peaks in the Cr5Cu20Fe25Mn25Ni25 and Al5Cu20Fe25Mn25Ni25 powders show, that the conditions of the mechanical alloying process didn't suffice for a full homogenization.

To identify the possible variation between the calculated crystal structure, cross-sections of the mechanically alloyed powders were manufactured and analysed via SEM and EDS. Fig. 3 displays cross section BSE images of the mechanically alloyed powders. Every particle inherits pores of varying sizes and shapes. The pore sizes and distribution increased in the bcc HEA Al30Cu30Fe5Mn25Ni10. Due to the small particle size some of the particles seem to be completely hollow. The porosity in the particles indicate a not fully homogenized state. In Fig. 3 b) particles with a rectangle shape and a lamellar texture can be seen also indicating a not fully homogenized state.

Table 4 shows the arithmetic mean and standard deviation of three EDS measurements of the powders shown in Fig. 3. A

Table 4 – EDS measurements of the mechanically alloyed powders.

	Al	Cr	Cu	Fe	Mn	Ni
Alloy	[At.-%]					
Al30Cu30Fe5Mn25Ni10	42.3 ± 1.2	–	32.0 ± 1.4	5.4 ± 0.2	9.8 ± 2.4	10.5 ± 0.1
Al11.25Cu35Fe5Mn20Ni28.75	16.1 ± 0.7	–	34.1 ± 2.4	6.0 ± 0.6	15.9 ± 5.3	27.9 ± 1.8
Al5Cu20Fe25Mn25Ni25	9.3 ± 1.7	–	20.8 ± 2.5	25.5 ± 1.1	21.2 ± 5.8	23.2 ± 3.4
Cr5Cu20Fe25Mn25Ni25	–	5.1 ± 0.2	20.2 ± 0.8	26.1 ± 0.7	23.0 ± 2.4	25.6 ± 0.8

significant variation is seen in the alloy Al30Cu30FeMn25Ni10. While the contents of Cu, Fe and Ni are in or near the nominal state, the contents of Al and Mn vary significantly. The Al content is 12.3 At.-% higher than the nominal state while the Mn content is up to 15 At.-% lower. The other alloys vary also in the Mn content but not as severe as the Al30Cu30-FeMn25Ni10 powder. The low Mn content explains the α-Mn peaks in the mechanically alloyed powders, especially the intense peak of the alloy Al30Cu30FeMn25Ni10. The reduced Mn content of the alloys in combination with the XRD pattern confirms the hypothesis that some of the particles weren't alloyed at all. Additionally, in the left-hand side of Fig. 3 b) a particle with a lamellar structure can be seen. These structures are common in mechanically alloyed powders, which are not fully homogenized [46]. In contrast the chemical composition of the Cr5Cu20Fe25Mn25Ni25 powder deviates only in small amounts compared to the alloys of the Al–Cu–Fe–Mn–Ni system. Despite the increased difference in the chemical composition of the alloys in the Al–Cu–Fe–Mn–Ni system the variation of the melting interval between simulation and experiment shown in Table 3 is as high as Cr5Cu20Fe25Mn25Ni25.

3.3. *Hot-pressing*

The mechanically alloyed powders were consolidated by the means of hot pressing. To analyse the change in crystal structure additional XRD-patterns are shown in Fig. 4.

The first obvious changes in comparison with the measured powders are the less broad peaks and the existence of M–II–Oxides and boron nitride. The latter is measured due to the usage of boron nitride as parting agent in the hot-pressing process. In every investigated XRD-pattern some peaks of oxide structures and boron nitride can be seen. The oxygen needed to form the detected oxides could come from different sources. Some oxygen is dissolved in the powders

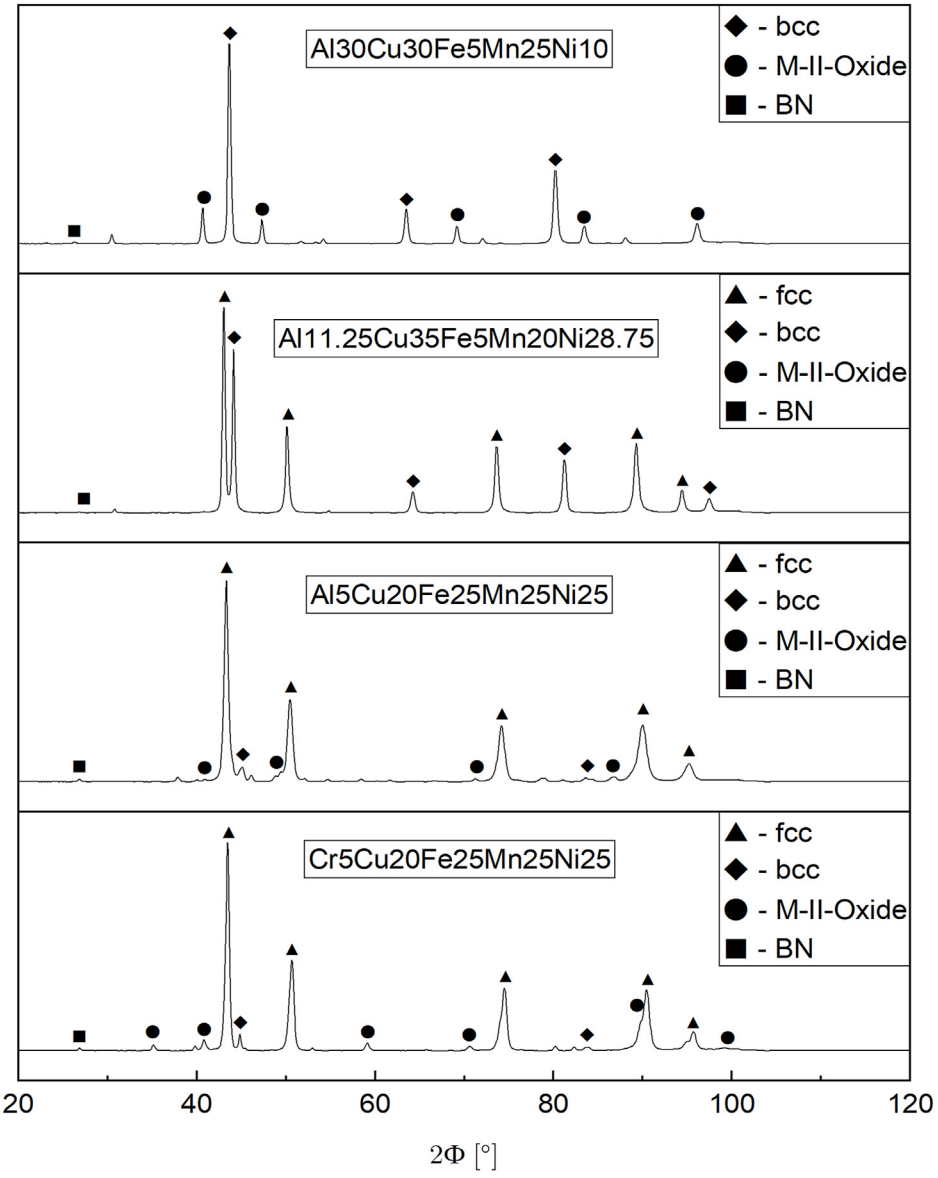

Fig. 4 – XRD patterns of the hot-pressed powders at 800 °C for 3 min: a) Al30Cu30Fe5Mn25Ni10; b) Al11.25Cu35Fe5Mn20Ni28.75; c) Al5Cu20Fe25Mn25Ni25 and d) Cr5Cu20Fe25Mn25Ni25.

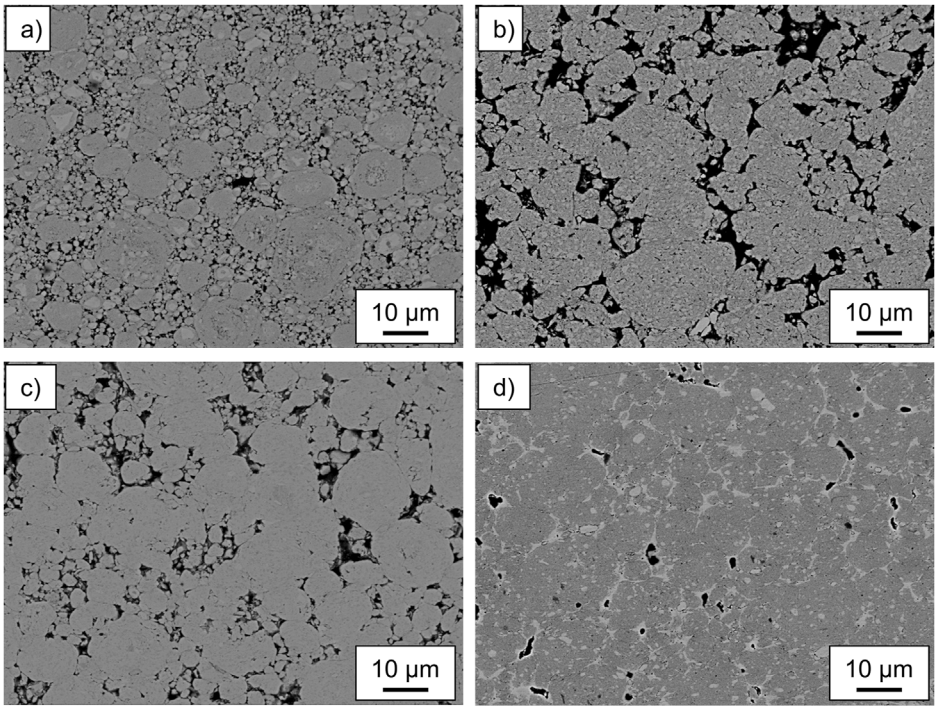

Fig. 5 – BSE images of the hot-pressed alloys at 800 °C for 3 min: a) Al30Cu30Fe5Mn25Ni10; b) Al11.25Cu35Fe5Mn20Ni28.75; c) Al5Cu20Fe25Mn25Ni25 and d) Cr5Cu20Fe25Mn25Ni25.

used for the mechanical alloying. It is known that mechanical alloying can produce amorphous structures. Therefore, the oxides could have been in the mechanically alloyed particles but would not be detected by the synchrotron radiation. Additionally, a very low percentage of oxygen is in the argon protection gas stream. The reason why oxides peaks were detected in the alloys Al30Cu30Fe5Mn25Ni10 and Al5Cu20-Fe25Mn25Ni25 but not in the alloy Al11.25Cu35-Fe5Mn20Ni28.75 cannot be explained yet and needs further investigations. Comparing the powder and hot-pressed XRD-patterns of the alloy Al30Cu30Fe5Mn25Ni the α-Mn peaks are completely vanished and only a bcc solid solution remains. Additionally, the M–II–Oxide peaks are the most intense in this alloy. The high amount of remaining pure Mn in the powder in addition to the very low particle size can increase the formation of oxides. Additionally, the high porosity of this alloy seen in Fig. 5 and noted in Table 5 indicate, that these hot-pressed samples have an open porosity. This can also increase the formation of oxides, due to the higher availability of oxygen out of the argon stream. Overall, comparing the XRD patterns of the hot-pressed alloys with the phase fraction diagrams shown in Fig. 1, the high temperature solid solutions simulated with Thermo-Calc could be verified.

Fig. 5 displays the cross-sections of the hot-pressed samples. The corresponding microhardness, macrohardness and porosity are displayed in Table 6. Al30Cu30Fe5Mn25Ni10 with its full bcc solid solution and Al11.25Cu35Fe5Mn20Ni28.75 with its partially bcc eutectic structure have the highest porosity. The results of the porosity should always be read with the particle size and melting interval in mind. Al30Cu30Fe5Mn25Ni10 showed a smaller particle size distribution than the other powders, which can lead to pores filled with small particles, which can distort the measurement. As mentioned in the materials and methods section, the porosity was measured by the means of light microscopy. Due to the small particle size, not every small pore could be detected, so

Table 5 – Hardness and porosity of the hot-pressed alloys and cobalt at 800 °C for 3 min.

	Microhardness		Macrohardness		Porosity	
	HV0.1		HV10		[Vol.-%]	
	$\bar{x}$	$\bar{s}$	$\bar{x}$	$\bar{s}$	$\bar{x}$	$\bar{s}$
Al30Cu30Fe5Mn25Ni10	623.49	81.1	425.22	3.68	11.59	2.94
Al11.25Cu35Fe5Mn20Ni28.75	373.89	90.94	227.34	22.73	11.05	1.65
Al5Cu20Fe25Mn25Ni25	429.63	77.85	264.66	33.34	8.56	1.07
Cr5Cu20Fe25Mn25Ni25	458.48	32.08	407.01	30.83	2.72	1.64
Diacob 1600 (Pure cobalt) [21]	–	–	107	–	1.35	–

Table 6 – EDS measurements of the-hot pressed alloys.

	Al	Cr	Cu	Fe	Mn	Ni
Alloy	[At.-%]					
Al30Cu30Fe5Mn25Ni10	34.6 ± 0.48	–	27.7 ± 0.36	5.4 ± 0.08	22.9 ± 0.12	9.5 ± 0.06
Al11.25Cu35Fe5Mn20Ni28.75	15.4 ± 0.24	–	32.4 ± 0.32	5.8 ± 0.15	19.3 ± 0.09	27.2 ± 0.14
Al5Cu20Fe25Mn25Ni25	7.5 ± 0.09	–	19.8 ± 0.10	24.5 ± 0.18	23.8 ± 0.22	24.4 ± 0.17
Cr5Cu20Fe25Mn25Ni25	–	5.1 ± 0.10	19.8 ± 0.17	25.7 ± 0.21	24.7 ± 0.14	24.7 ± 0.07

Table 7 – Phase composition of the three phases which exist at 700 °C in the phase fraction diagram of Cr5Cu20Fe25Mn25Ni25 shown in Table 1 d).

Cr5Cu20Fe25Mn25Ni25		Cr	Cu	Fe	Mn	Ni
Phase	Vol.-%	[At.-%]				
FCC_L12#1	91	2.14	20.90	24.59	24.47	27.90
FCC_L12#2	3	0.15	65.68	2.54	17.44	14.19
SIGMA#1	6	30.13	–	34.56	31.48	3.83

the porosity might be higher than the measured value. These results show that a higher value of the bcc solid solution or a fully bcc HEA has reduced consolidation properties than an alloy with a higher amount or only fcc structures. The high standard deviation of the hardness measurements of the alloys in the Al–Cu–Fe–Mn–Ni system can be attributed to the high porosity. Some hardness indents were distorted by nearby pores. Al30Cu30Fe5Mn25Ni10 had a high overall porosity, but the pores have a fine distribution resulting in a less varying macrohardness. Nonetheless, the macrohardness is lower than the microhardness. Cr5Cu20Mn25Fe25Ni25 on the other hand showed a significant lower porosity than Al5Cu20Fe25Mn25Ni25, resulting also in a lower standard deviation in the hardness measurements and a higher macrohardness. As shown in Fig. 5 d) a second phase precipitated in the microstructure. Around every pore in the shown BSE image of Cr5Cu20Fe25Mn25Ni25 this second phase precipitated. Additionally, the hardness and porosity of pure cobalt (Diacob 1600 by Dr. Fritsch) is shown in Table 5. The porosity of this alloy was measured by the Archimedes method. This method includes every pore and oxide in the sample, resulting in a higher and more accurate value of the porosity than the optical measurements done for the HEA and CCA. This shows, that pure cobalt has better consolidation properties then the HEA and CCA but lacks significantly in hardness.

Additionally, to hardness and porosity the chemical composition was measured by EDS. Three EDS area measurements were taken at a magnification of ×200. The arithmetic mean and standard deviation are displayed in Table 7. The results show a better homogenization which was expected due to the diffusion in the hot-pressing process. But the Al content of the alloys in the Al–Cu–Fe–Mn–Ni system is still significantly increased compared to the nominal composition. Additional EDS-spots were taken to identify local differences in the chemical composition, except for Al11.25Cu35Fe5Mn20Ni28.75 due to the two solid solutions, no

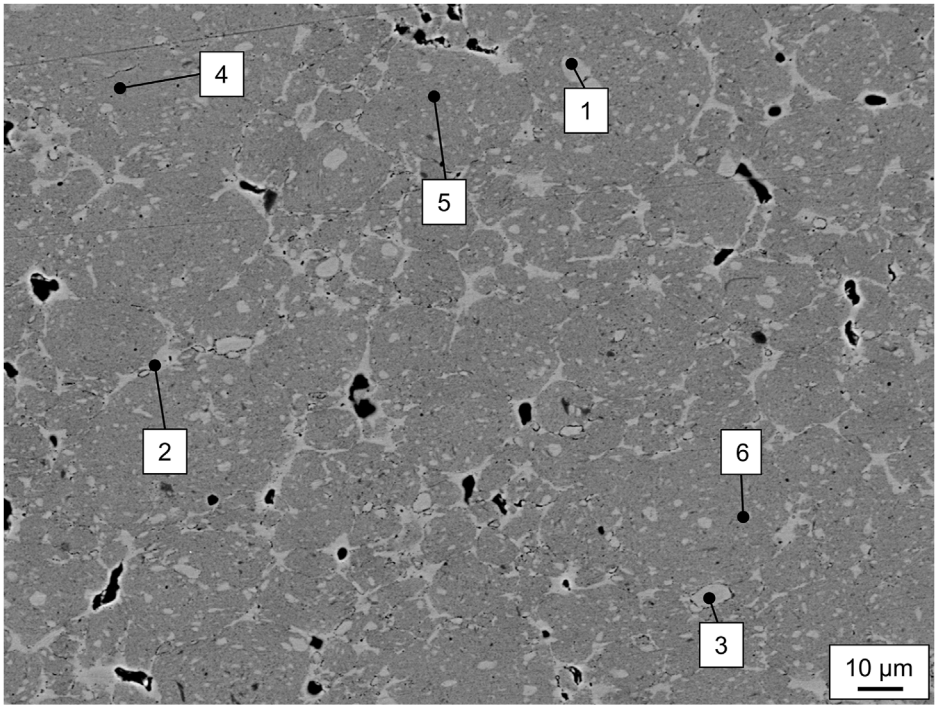

Fig. 6 – EDS measurements of Cr5Cu20Fe25Mn25Ni25 hot-pressed at 800 °C for 3 min.

Table 8 – EDS measurements of Cr5Cu20Fe25Mn25Ni25.

Cr5Cu20Fe25Mn25Ni25					
No.	Cr	Cu	Fe	Mn	Ni
[-]			[At.-%]		
1	0.67	40.89	10.69	22.76	24.99
2	0.91	42.16	10.83	22.34	23.76
3	0.46	42.11	9.21	23.21	25.00
4	4.51	16.16	28.94	24.39	25.99
5	4.24	14.71	30.34	24.62	26.09
6	5.47	15.32	29.62	24.64	24.95

variation could be found that would explain the difference between the measurements in Table 6 in comparison with the nominal composition. Cr5Cu20Fe25Mn25Ni25 on the other hand shows almost the nominal composition. This leads to the conclusion that Al has a different interaction with the steel balls and the vial during the ball milling process. After the process the balls and vials showed a patina. An explanation for the varying chemical composition is, that Al has a slightly smaller reaction withs the ball or vial material. This results in a higher Al concentration in the resulting powders and hot-press samples.

In the XRD pattern of Cr5Cu20Fe25Mn25Ni25 no additional solid solution or intermetallic phase could be detected. The second phase features most probably a fcc structure, as predicted in the simulation shown as line 4 in Fig. 1 d). Additionally, a sigma phase was also predicted which was not detected via the XRD measurement. This confirms the theory, that alloys with a higher entropy are more stable and tend to form solid solutions over intermetallic phases. It is also to mention, that the simulation calculates the thermodynamic equilibrium. This is at a theoretical infinite long annealing process at the given temperature. Mechanical alloying and hot pressing are two manufacturing processes far from the thermodynamic equilibrium. This can also attribute to the lack of sigma phase in this alloy. Nonetheless, the simulation can give a hint which crystal structure the second phase has. So, in Table 7 the chemical composition of the three phases existing in the phase fraction diagram shown in Fig. 1 d) is noted.

The results show, that the second fcc phase has a higher concentration of copper. These type of copper rich fcc-structures are also known in alloys like $Al_xCoCrCuFeNi$ or CoCrCuFeNi [3,47]. To verify that this phase is rich in copper EDS measurements were done. The point measurements are shown in Fig. 6 with the results in Table 8.

Number 1–3 are measurements in the light grey phase. The composition indicates a higher Cu and lower Fe and Cr content compared to the nominal chemical composition. This effect is based on the positive enthalpy of mixing of Cu with Cr and Fe [44]. The darker grey phase has a lower Cu and an increased Fe content confirming the hypothesis. This is indicated by the

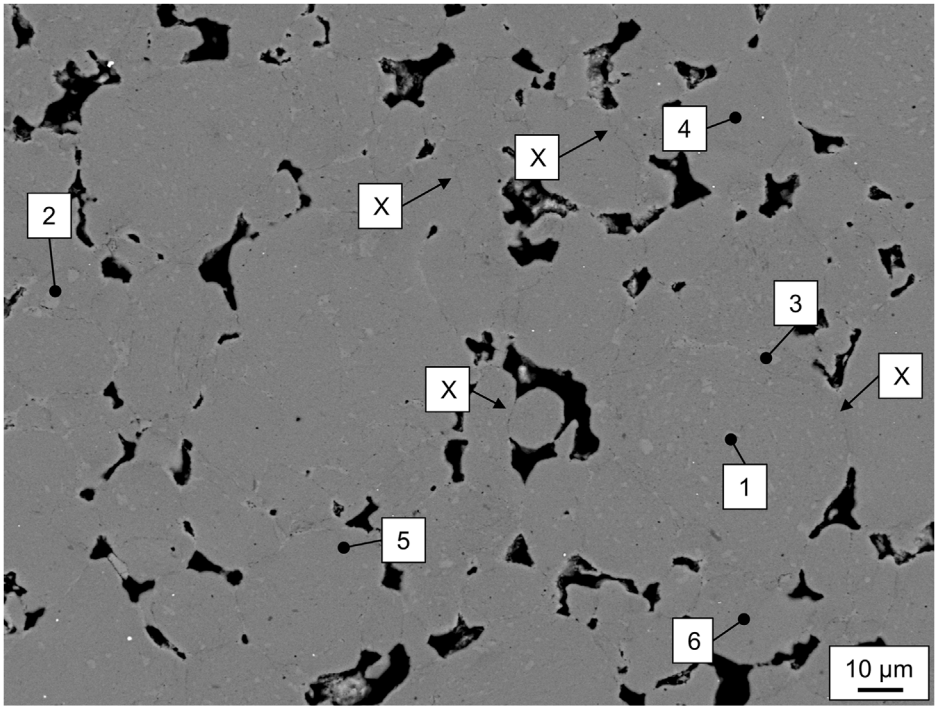

Fig. 7 – EDS measurements of Cr5Cu15Fe25Mn25Ni30 hot-pressed at 800 °C for 3 min.

Table 9 – Comparison of the particle size and melting range of Cr5Cu20Fe25Mn25Ni25 and Cr5Cu15Fe25Mn25Ni30.

	Particle size			Melting range			
				Simulation		DTA	
	d_{10}	d_{50}	d_{90}	T_L	T_S	T_L	T_S
Alloy	[μm]			[°C]			
Cr5Cu20Fe25Mn25Ni25	3.76	6.23	13.44	1201	1100	1258	1051
Cr5Cu15Fe25Mn25Ni30	4.99	8.27	17.57	1211	1128	1245	1096

varying Cu, Fe and Cr contents between the two phases and confirms the concentrations of the different phases by the thermodynamic calculations. The copper rich phase precipitates around the pores of the hot-pressed sample. In relation with the higher porosity of Al5Cu20Fe25Mn25Ni25 which lacks a second copper rich phase, the hypothesis emerges that the copper rich phase is responsible for the good consolidation properties of Cr5Cu20Fe25Mn25Ni25.

To verify this, a fifth alloy with a lower Cu content was mechanically alloyed. This alloy is Cr5Cu15Fe25Mn25Ni30. The higher Ni content was chosen due to the small variation in the EDS measurements shown in Table 8 and the negative enthalpy of mixing between Ni and Cu [44]. A BSE image with EDS measurements of this alloy is shown in Fig. 7.

In the BSE image the porosity is increased while the light grey copper rich phase measured in the EDX spots 1 to 3 is decreased has a lower volume fraction in comparison with Cr5Cu20Fe25Mn25Ni25. The spots marked with an X seem to be microcracks, but at a higher magnification these lines show the initial boundary of the powder particles. To validate that the consolidation properties of Cr5Cu20Fe25Mn25Ni25 are higher due to the higher copper content the melting range and particle size need to be compared. In Table 9 the experimental and simulated melting range as well as the particle size of both alloys are noted.

The particle size of Cr5Cu15Fe25Mn25Ni30 is comparable to the particle size of Cr5Cu20Fe25Mn25Ni25 as well as the simulated and experimental melting range. So, the external factors are nearly identical. The measured EDS spots in Fig. 7 are displayed in Table 10. The spots 1–3 measured the light grey area. Some of these areas were very small, so some of the surrounding dark grey areas were also measured. But it can be seen that the content of Fe and Cr are reduced as well as an increased amount of Cu. The spot measures 4–6 show only a slight increase in Cr and Fe. This is due to the low volume fraction of the Cu rich phase. The hardness and porosity values are on the same level as Al5Cu20Fe25Mn25Ni25. Both alloys consist mostly of a single solid solution. So, the hypothesis, that the increased volume of the Cu-rich phase in Cr5Cu20Fe25Mn25Ni25 is responsible for the low porosity is verified by these observations.

3.4. *Diamond metal-matrix composites*

In addition to the consolidation properties of the investigated HEA and CCA, the interaction with diamonds was also investigated. As mentioned in the materials and methods section the hot-pressing temperature was raised to 900 °C to simulate an industrial process and to investigate a potential reaction with diamonds. The XRD patterns of the investigated alloys hot-pressed at 900 °C for 3 min with diamonds are shown in Fig. 8.

The XRD patterns show the same solid solution peaks for the HEA and CCA as described for the hot-pressed samples without diamonds in Fig. 4. Additionally, no peaks for diamond, graphite or carbides were detected. The lack of diamond peaks can be attributed to the mono crystallinity of the used diamonds. The synchrotron radiation was emitted in only one angle onto the samples. A diamond peak only occurs if the crystal structure was aligned with the emitted radiation, which was not the case in the investigated samples. But no graphite or carbides could be detected. These structures are polycrystalline and do not need to be aligned perfectly to create a peak. It is also to mention, that only the surface of the sample was tested, and it is possible that some amorphous structures or nano-scale carbide layers would not be detected. To get additional information about the reaction between the diamonds and the different metal matrixes SEM analysed of the samples were conducted. For this purpose, the samples were cooled down by liquid nitrogen and broken instead of cutting a machining cross section. The SEM analyses were carried out on the fractured surfaces.

Table 10 – EDS measurements, porosity, micro- and macrohardness of Cr5Cu15Fe25Mn25Ni30.

Cr5Cu15Fe25Mn25Ni30						Microhardness		Macrohardness		Porosity	
No.	Cr	Cu	Fe	Mn	Ni	HV0.1		HV10		[Vol.-%]	
[-]	[At.-%]					x	s	x	s	x	s
1	0.99	34.45	11.43	23.60	29.54	442.14	92.33	317.96	13.07	8.21	0.87
2	1.24	31.63	11.89	24.53	30.70						
3	2.10	30.08	14.46	22.82	30.54						
4	5.89	13.16	27.87	23.93	29.15						
5	5.39	13.96	26.84	24.63	29.17						
6	6.44	11.53	28.64	25.84	27.54						

Fig. 9 shows the BSE images of all four hot-pressed alloys with diamonds. The diamonds within the images feature sharp edges, which is an indication for the absence of a superficial formation of carbides of graphite in the hot-presses state. Additionally, in Fig. 9 c) some areas are visible, in which the diamonds fell out of the sample. This also indicates that no reaction layer was formed between alloy and diamonds. The images b) and c) also show a remaining porosity, which could also hinder the reaction between the diamonds and the matrix. Due to the high consolidation properties of Cr5Cu20Fe25Mn25Ni25 and the Cr content which is known to form carbides in contact with diamonds [39,40] this alloy is analysed further in the following section to gain additional insights on the diamond interaction.

3.5. *Cr5Cu20Fe25Mn25Ni25*

In Fig. 10 varying BSE images are shown. These show samples without diamonds and varying hot-pressing parameters to identify the influence of longer holding times and higher temperatures. The hardness values and the porosity of the samples are noted in Table 11.

At a temperature of 900 °C no porosity could be measured via optical microscopy. With a reduced porosity the hardness increased. The highest hardness value was achieved at 5 min at 900 °C with 462 HV. This exceeds the hardness of pure hot-pressed cobalt [21] by factor 4.3 and an experimental Fe-Mn-Cu-Sn [22] alloy by factor 1.31. At higher hot-pressing times and temperatures, the hardness value is reduced. This can be

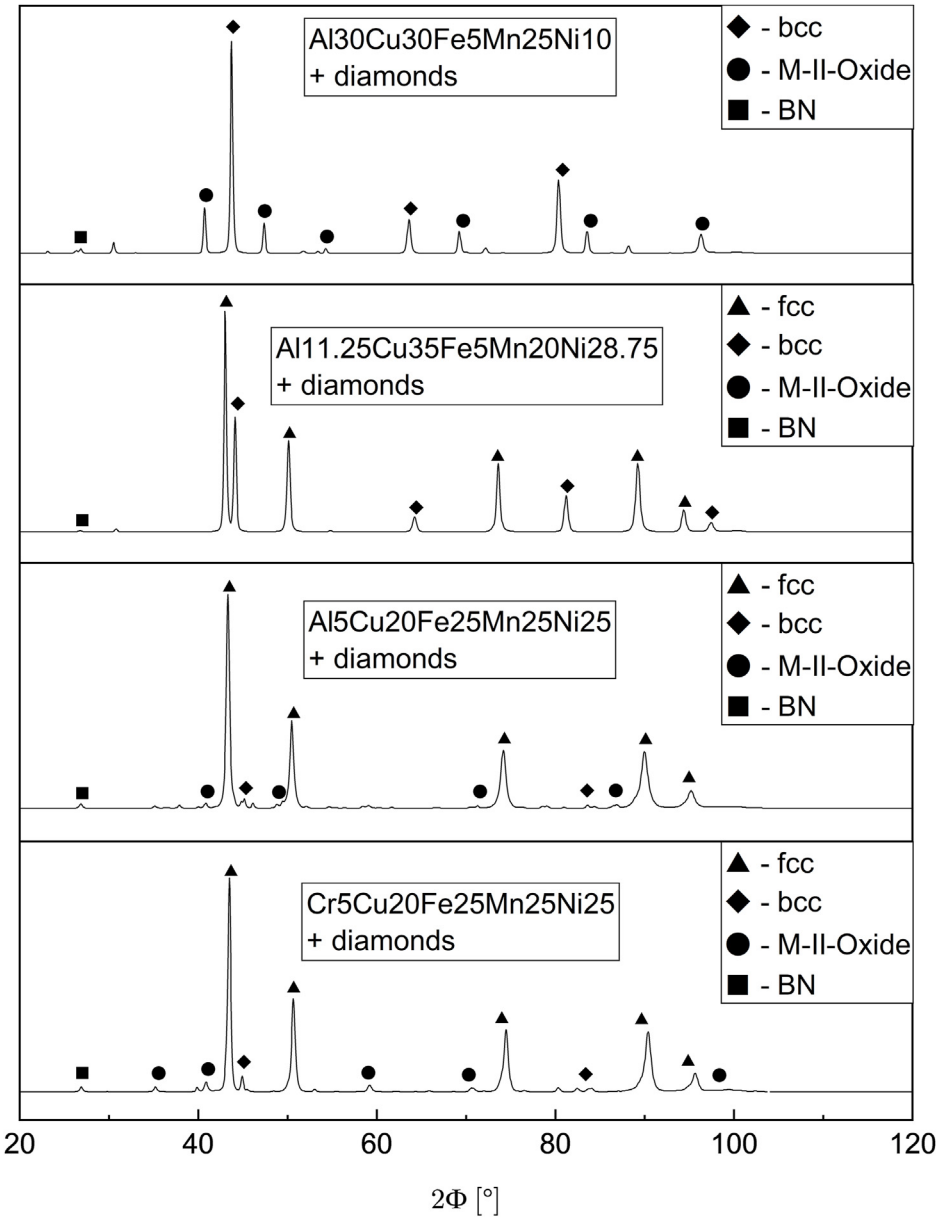

Fig. 8 – XRD patterns of the hot-pressed alloys with diamonds at 900 °C for 3 min: a) Al30Cu30Fe5Mn25Ni10; b) Al11.25Cu35Fe5Mn20Ni28.75; c) Al5Cu20Fe25Mn25Ni25 and d) Cr5Cu20Fe25Mn25Ni25.

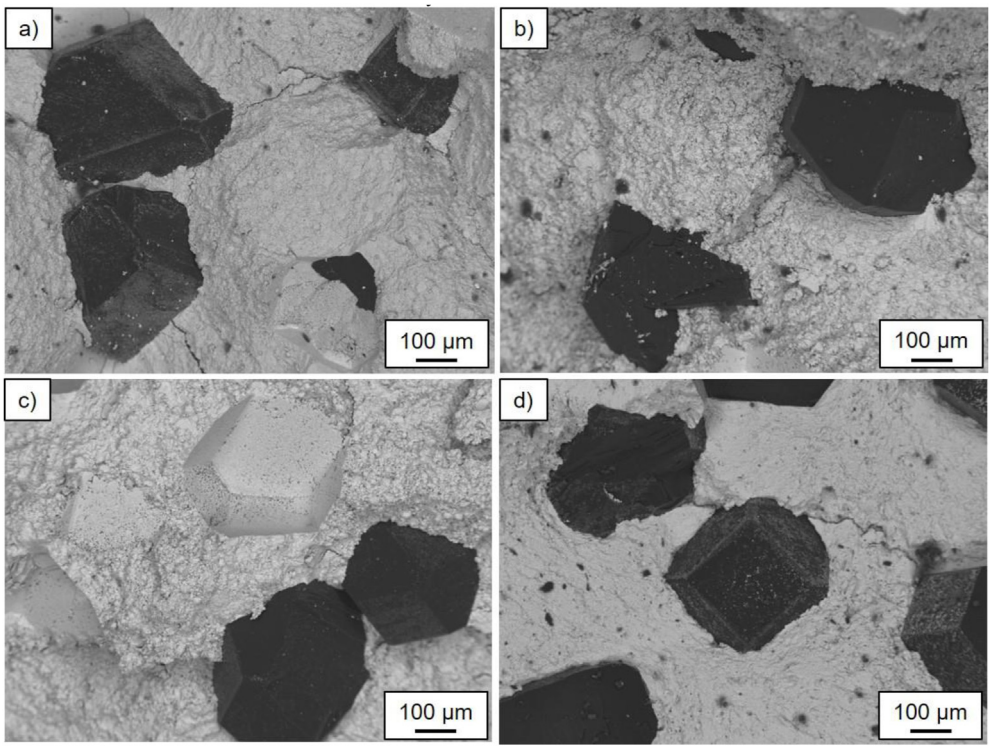

Fig. 9 – BSE images of the hot-pressed alloys with diamonds at 900 °C for 3 min: a) Al30Cu30Fe5Mn25Ni10; b) Al11.25Cu35Fe5Mn20Ni28.75; c) Al5Cu20Fe25Mn25Ni25 and d) Cr5Cu20Fe25Mn25Ni25.

contributed to the slightly reduced amount of copper rich phase in the samples. Also, at higher temperatures and hot-pressing times the number of oxides increases. It is also to mention, that the hardness values at 5 min for 800 °C and 900 °C vary only slightly. This could be interesting for a possible application in industrial processes, where the optimal hot-pressing parameters are in between this temperature range for around 5 min isothermal consolidation.

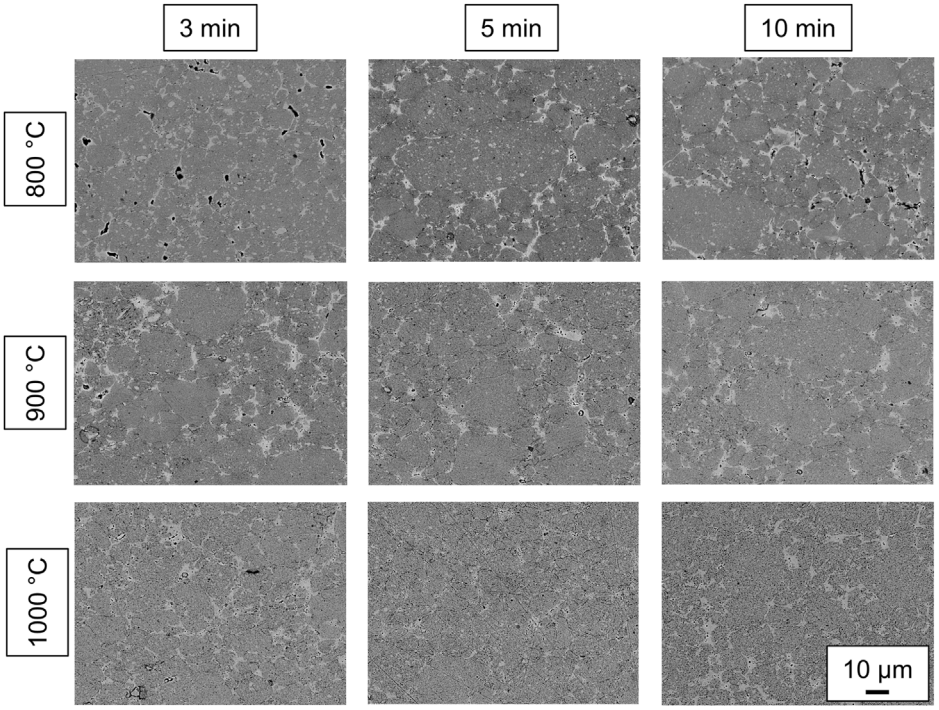

Fig. 10 – BSE images of the temperature and time variation of hot-pressed Cr5Cu20Fe25Mn25Ni25 samples.

Table 11 – Macrohardness and porosity of the time and temperature variation of Cr5Cu20Fe25Mn25Ni25.

	Cr5Cu20Fe25Mn25Ni25					
	Macrohardness			Porosity		
	HV10			[Vol.-%]		
	3 min	5 min	10 min	3 min	5 min	10 min
800 °C	407 ± 27.6	455 ± 5.8	429 ± 11.7	2.72 ± 1.2	0.12 ± 0.03	0.62 ± 0.19
900 °C	428 ± 3.6	462 ± 4.6	410 ± 2.5	0.02 ± 0.03	0.01 ± 0.01	0.02 ± 0.01
1000 °C	436 ± 3.6	410 ± 3.7	405 ± 6.0	0.00 + 0.01	0.00 ± 0.00	0.00 ± 0.00

On the first glance of the XRD pattern and the first SEM pictures no interaction between the diamonds and the investigated HEA and CCA could be seen. Fig. 11 shows a higher resolution SE-image with residue and pores on the surface of a diamond embedded in a Cr5Cu20Fe25Mn25Ni25 matrix hot-pressed at 900 °C.

The secondary electrons (SE) are from within a few nanometres below the surface. So, the SE image in Fig. 11 gives an example of the surface topography of a diamond. There are some darker areas which lie deeper within the diamond indicating some kind of pores or fractured surface layer, while the brighter spots can be residue of a reaction zone. Also the pores an indicate some kind of reaction zone which broke off while preparing the sample. To get deeper insight Fig. 12 shows a BSE image of the residue marked as Fig. 12 in Fig. 11.

The BSE image at a high magnification cements the impression, that a reaction happened between the diamond and the matrix. In the darker areas of the diamond there are networks of brighter areas which indicate residues of the matrix material. The darker areas show the pores identified in Fig. 11. The network of residue shows that while the sample was prepared via breaking the reaction layer fractured and created these pores. Two EDS measurements of the residues were taken and are noted with and without the carbon content shown in Table 12. Without the carbon content it is clear, that a higher Fe and Mn concentration are within the residue in comparison with Cr, Cu and Ni. Fe and Mn can form carbides [48,49] but in contact with diamonds they increase the graphitization instead of forming carbides [39]. For a clear identification of carbides, a higher concentration of chromium could be an indicator. But the normalised values are lower

Table 12 – EDS measurements of Fig. 12 with and without the carbon content.

Cr5Cu20Fe25Mn25Ni25 with diamonds						
No.	C	Cr	Cu	Fe	Mn	Ni
[-]				[At.-%]		
1	71.32	1.25	3.14	11.67	9.21	3.40
2	47.26	2.47	7.51	19.14	15.91	7.72
Normalised without C content						
1	–	4.35	10.96	40.69	32.12	11.86
2	–	4.68	14.23	36.29	30.16	14.64

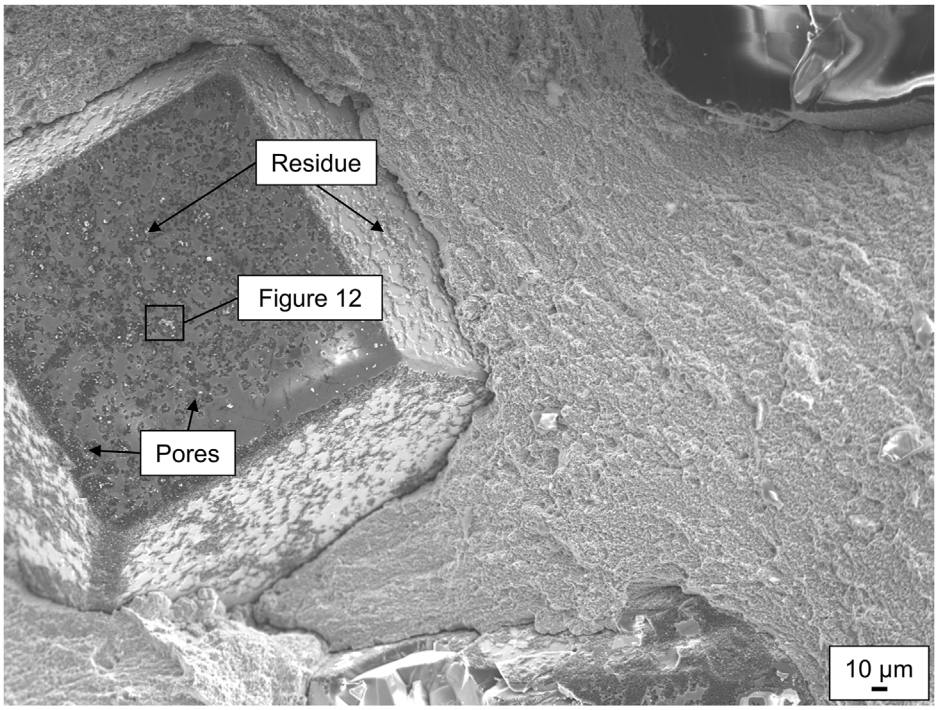

Fig. 11 – SE images of the Cr5Cu20Fe25Mn25Ni25 sample hot-pressed at 900 °C for 3 min.

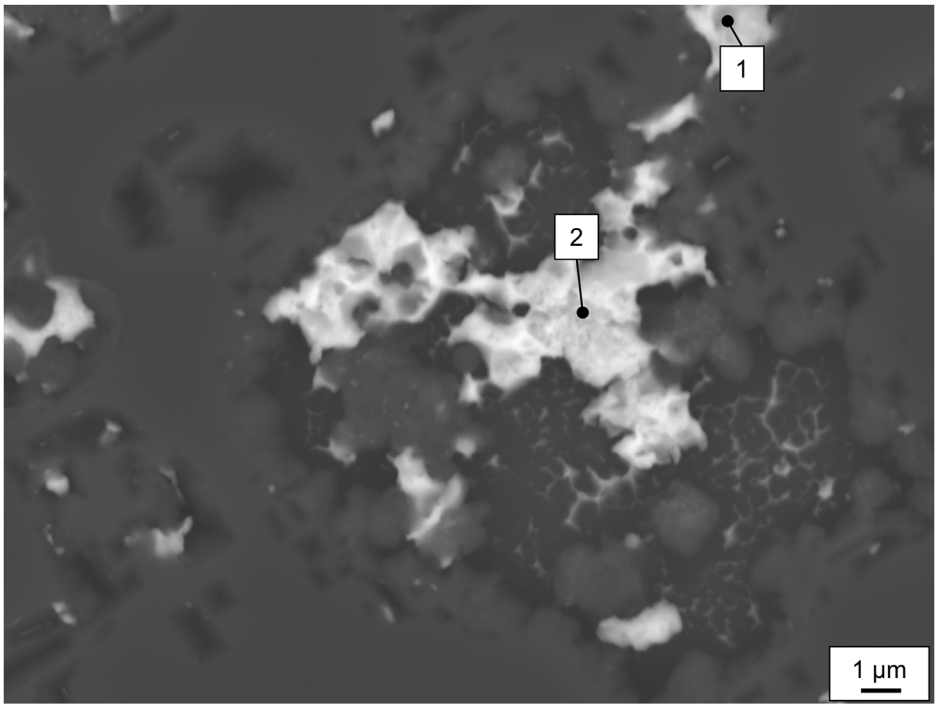

Fig. 12 – BSE images of the temperature and time variation of hot-pressed Cr5Cu20Fe25Mn25Ni25 samples.

than the nominal concentration of the alloy. To confirm the creation of carbides further investigation is necessary. A slight graphitization can be seen due to the pores on the surface of the diamonds.

4. Conclusions

The aim of this research was to identify a HEA or CCA without cobalt for an application as metal matrix in diamond impregnated tools. Within this investigation the focus was on the selection of an appropriate alloy composition, the consolidation properties by the means of hot-pressing and the interaction with diamonds of these alloys. Additionally, the influence of varying crystal structures on the consolidation properties were analysed as well. The alloys Al30Cu30Fe5Mn25Ni10, Al11.25Cu35Fe5Mn20Ni28.75, Al5Cu20Fe25Mn25Ni25 and Cr5Cu20Fe25Mn25Ni25 were chosen based on the crystal structure and melting temperature shown in phase fraction diagrams calculated with Thermo-Calc. The results can be concluded in the following points.

(I) The alloys containing Al need a higher energy input for mechanical alloying to achieve a fully homogenized state or a concentration slightly below the nominal state due to a reduced reactivity, in comparison with the other used elements, with the ball and vial materials.

(II) Three of the four investigated alloys showed an almost full fcc crystal structure after mechanical alloying with slight indications of a bcc crystal structure. This was due to residues of unalloyed powder particles.

(III) The hot-pressed samples showed a higher homogenization as the mechanically alloyed powders. The Al containing alloys had a higher deviation in the chemical composition.

(IV) The phase fraction diagrams of Al30Cu30Fe5Mn25Ni10 and Cr5Cu20Fe25Mn25Ni25 showed intermetallic phases in the investigated temperature range, but none of these phases precipitated. This is contributed to the high entropy of these alloys.

(V) A higher bcc content in the alloy showed a higher porosity. The best consolidation properties were shown by Cr5Cu20Fe25Mn25Ni25. A second copper-rich fcc phase precipitated around the pores resulting in a significant reduction of the porosity. A fifth alloy Cr5Cu15Fe25Mn25Ni30 was created to verify this point. It showed almost none of the copper-rich phase resulting in a porosity in the range of Al5Cu20Fe25Mn25Ni25.

(VI) Cr5Cu20Fe25Mn25Ni25 can be fully consolidated between 800 °C and 900 °C at 5 min isothermal holding time. The hardness achieves a maximum value of 462 HV10 exceeding pure cobalt by factor 4.3.

(VII) The created XRD-patterns of the hot-pressed diamond metal matrix composites showed no sign of carbide or graphite formation, as well as low magnification SEM images. At a higher magnification the samples with Cr5Cu20Fe25Mn25Ni25 and diamonds hot-pressed at 900 °C for 3 min showed some kind of reaction with the diamonds. Pores near the surface and residue if the matrix material indicate some form of reaction. To identify if carbides or graphite formed additional experiments must be made.

Cr5Cu20Fe25Mn25Ni25 showed the highest potential as a metal-matrix for diamond tools. To clarify if carbides and graphite form on the interface, an XRD measurement needs to be taken without the matrix. This can be done by dissolving the metal matrix via an acid. Additionally, three-point bending tests can be done to identify the mechanical properties in addition to the hardness. The evaluation of a higher Cu content can identify an alloy with even higher consolidation properties due to an increased volume fraction of the copper rich fcc phase. With a higher Cr content, a possible carbide reaction layer can be created or increased to influence the performance of these tools. All in all, fcc HEA and CCA seem to have a great potential as cobalt free metal-matrixes for diamond tools.

Declaration of Competing Interest

The authors declare that they have no known competing financial interests or personal relationships that could have appeared to influence the work reported in this paper.

Acknowledgements

The authors thank the DELTA machine group especially Christian Sternemann for providing the synchrotron radiation within the Beamline 9 and the analysis of the diffraction data. We also acknowledge financial support by Deutsche Forschungsgemeinschaft and Technische Universität Dortmund/TU Dortmund University within the funding programme Open Access Costs.

REFERENCES

[1] Cantor B, Chang I, Knight P, Vincent A. Microstructural development in equiatomic multicomponent alloys. Mater Sci Eng, A 2004;375–377:213–8. https://doi.org/10.1016/j.msea.2003.10.257.

[2] Yeh J-W, Chen S-K, Lin S-J, Gan J-Y, Chin T-S, Shun T-T, et al. Nanostructured high-entropy alloys with multiple principal elements: novel alloy design concepts and outcomes. Adv Eng Mater 2004;6(5):299–303.

[3] Tong C-J, Chen M-R, Yeh J-W, Lin S-J, Chen S-K, Shun T-T, et al. Mechanical performance of the Al x CoCrCuFeNi high-entropy alloy system with multiprincipal elements. Metall Mater Trans 2005;36(5):1263–71. https://doi.org/10.1007/s11661-005-0218-9.

[4] Wang W-R, Wang W-L, Yeh J-W. Phases, microstructure and mechanical properties of AlxCoCrFeNi high-entropy alloys at elevated temperatures. J Alloys Compd 2014;589:143–52. https://doi.org/10.1016/j.jallcom.2013.11.084.

[5] Hsu C-Y, Yeh J-W, Chen S-K, Shun T-T. Wear resistance and high-temperature compression strength of Fcc CuCoNiCrAl0.5Fe alloy with boron addition. Metall Mater Trans 2004;35(5):1465–9. https://doi.org/10.1007/s11661-004-0254-x.

[6] Chuang M-H, Tsai M-H, Wang W-R, Lin S-J, Yeh J-W. Microstructure and wear behavior of AlxCo1.5CrFeNi1.5Tiy high-entropy alloys. Acta Mater 2011;59(16):6308–17. https://doi.org/10.1016/j.actamat.2011.06.041.

[7] Guo NN, Wang L, Luo LS, Li XZ, Chen RR, Su YQ, et al. Hot deformation characteristics and dynamic recrystallization of the MoNbHfZrTi refractory high-entropy alloy. Mater Sci Eng, A 2016;651:698–707. https://doi.org/10.1016/j.msea.2015.10.113.

[8] Chou YL, Wang YC, Yeh JW, Shih HC. Pitting corrosion of the high-entropy alloy Co1.5CrFeNi1.5Ti0.5Mo0.1 in chloride-containing sulphate solutions. Corrosion Sci 2010;52(10):3481–91. https://doi.org/10.1016/j.corsci.2010.06.025.

[9] Denkena B, Tönshoff HK, Friemuth T, Gierse A, Glatzel T, Hillmann-Apmann H. Innovative trennschleifprozesse in der Natursteinbearbeitung. Werkstatttechnik online 2002;92(6):290–6.

[10] Ozcelik Y, Polat E, Bayram F, Ay AM. Investigation of the effects of textural properties on marble cutting with diamond wire. Int J Rock Mech Min Sci 2004;41:228–34.

[11] Ozcelik Y, Yilmazkaya E. The effect of the rock anisotropy on the efficiency of diamond wire cutting machines. Int J Rock Mech Min Sci 2011;48(4):626–36.

[12] Konstanty J, Bunsch A. Hot pressing of cobalt powders. Powder Metall 1991;34(3):195–8. https://doi.org/10.1179/pom.1991.34.3.195.

[13] Ylikerälä J, Gasik M. Cobalt price hikes set search for alternates in train. Met Powder Rep 2004;59(9):36–9. https://doi.org/10.1016/S0026-0657(04)00255-3.

[14] Bastian S, Busch W, Kühnel D, Springer A, Meissner T, Holke R, et al. Toxicity of tungsten carbide and cobalt-doped tungsten carbide nanoparticles in mammalian cells in vitro. Environ Health Perspect 2009;117(4):530–6. https://doi.org/10.1289/ehp.0800121.

[15] Hou M, Guo S, Yang L, Gao J, Peng J, Hu T, et al. Fabrication of Fe–Cu matrix diamond composite by microwave hot pressing sintering. Powder Technol 2018;338:36–43. https://doi.org/10.1016/j.powtec.2018.06.043.

[16] Romański A. Factors affecting diamond retention in powder metallurgy diamond tools. Arch Metall Mater 2010;55(4). https://doi.org/10.2478/v10172-010-0009-1.

[17] Zhao X, Li J, Duan L, Tan S, Fang X. Effect of Fe-based pre-alloyed powder on the microstructure and holding strength of impregnated diamond bit matrix. Int J Refract Metals Hard Mater 2019;79:115–22. https://doi.org/10.1016/j.ijrmhm.2018.11.015.

[18] Hsieh Y-Z, Lin S-T. Diamond tool bits with iron alloys as the binding matrices. Mater Chem Phys 2001;72(2):121–5. https://doi.org/10.1016/S0254-0584(01)00419-9.

[19] Del Villar M, Muro P, Sánchez JM, Iturriza I, Castro F. Consolidation of diamond tools using Cu–Co–Fe based alloys as metallic binders. Powder Metall 2001;44(1):82–90. https://doi.org/10.1179/003258901666211.

[20] Huadong D, Yawen L, Hongqi H, Zhihao J. Decreasing the sintering temperature of diamond-bit matrix material by the addition of the element P. J Mater Process Technol 1998;74(1–3):52–5. https://doi.org/10.1016/S0924-0136(97)00248-3.

[21] Dr. Fritsch Sondermaschinen GmbH. Sinterdatenblatt diacob 1600. https://dr-fritsch.de/fileadmin/user_upload/downloads/sinterdatenblaetter/Sinter_Diacob-1600_DE.pdf.

[22] Konstanty JS, Baczek E, Romanski A, Tyrala D. Wear-resistant iron-based Mn–Cu–Sn matrix for sintered diamond tools. Powder Metall 2018;61(1):43–9. https://doi.org/10.1080/00325899.2017.1379737.

[23] Moravcik I, Cizek J, Zapletal J, Kovacova Z, Vesely J, Minarik P, et al. Microstructure and mechanical properties of Ni1,5Co1,5CrFeTi0,5 high entropy alloy fabricated by mechanical alloying and spark plasma sintering. Mater Des 2017;119:141–50. https://doi.org/10.1016/j.matdes.2017.01.036.

[24] Wang M, Cui H, Zhao Y, Wang C, Wei N, Zhao Y, et al. A simple strategy for fabrication of an FCC-based complex concentrated alloy coating with hierarchical nanoprecipitates and enhanced mechanical properties. Mater Des 2019;180:107893. https://doi.org/10.1016/j.matdes.2019.107893.
[25] Shang C, Axinte E, Sun J, Li X, Li P, Du J, et al. CoCrFeNi(W1−xMox) high-entropy alloy coatings with excellent mechanical properties and corrosion resistance prepared by mechanical alloying and hot pressing sintering. Mater Des 2017;117:193–202. https://doi.org/10.1016/j.matdes.2016.12.076.
[26] Zhang M, Zhang W, Liu Y, Liu B, Wang J. FeCoCrNiMo high-entropy alloys prepared by powder metallurgy processing for diamond tool applications. Powder Metall 2018;61(2):123–30. https://doi.org/10.1080/00325899.2018.1429044.
[27] Zhang W, Zhang M, Peng Y, Wang L, Liu Y, Hu S, et al. Interfacial structures and mechanical properties of a high entropy alloy-diamond composite. Int J Refract Metals Hard Mater 2020;86:105109. https://doi.org/10.1016/j.ijrmhm.2019.105109.
[28] Zhang W, Zhang M, Peng Y, Liu F, Liu Y, Hu S, et al. Effect of Ti/Ni coating of diamond particles on microstructure and properties of high-entropy alloy/diamond composites. Entropy 2019;21(2). https://doi.org/10.3390/e21020164.
[29] Peng YB, Zhang W, Mei XL, Wang HJ, Zhang MY, Wang L, et al. Microstructures and mechanical properties of FeCoCrNi-Mo High entropy alloys prepared by spark plasma sintering and vacuum hot-pressed sintering. Mater Today Commun 2020;24:101009. https://doi.org/10.1016/j.mtcomm.2020.101009.
[30] Andersson J-O, Helander T, Höglund L, Shi P, Sundman B. Thermo-Calc & DICTRA, computational tools for materials science. Calphad 2002;26(2):273–312.
[31] Mao H, Chen H-L, Chen Q. TCHEA1: a thermodynamic database not limited for "high entropy" alloys. J Phase Equilibria Diffus 2017;38(4):353–68. https://doi.org/10.1007/s11669-017-0570-7.
[32] Chen H-L, Mao H, Chen Q. Database development and Calphad calculations for high entropy alloys: challenges, strategies, and tips. Mater Chem Phys 2018;210:279–90. https://doi.org/10.1016/j.matchemphys.2017.07.082.
[33] Nguyen H-V, Kim J-S, Kwon Y-S, Kim J-C. Amorphous Ti–Cu–Ni–Al alloys prepared by mechanical alloying. J Mater Sci 2009;44(10):2700–4. https://doi.org/10.1007/s10853-009-3354-6.
[34] Praveen S, Murty BS, Kottada RS. Alloying behavior in multi-component AlCoCrCuFe and NiCoCrCuFe high entropy alloys. Mater Sci Eng, A 2012;534:83–9. https://doi.org/10.1016/j.msea.2011.11.044.
[35] Krywka C, Paulus M, Sternemann C, Volmer M, Remhof A, Nowak G, et al. The new diffractometer for surface X-ray diffraction at beamline BL9 of DELTA. J Synchrotron Radiat 2006;13(Pt 1):8–13. https://doi.org/10.1107/S0909049505035685.
[36] Hammersley AP, Svensson SO, Thompson A. Calibration and correction of spatial distortions in 2D detector systems. Nucl Instrum Methods Phys Res Sect A Accel Spectrom Detect Assoc Equip 1994;346(1–2):312–21.
[37] Tillmann W, Tolan M, Pinho Ferreira M, Paulus M, Becke M, Stangier D. X-ray diffraction (XRD)-studies on the temperature dependent interface reactions on hafnium, zirconium, and nickel coated monocrystalline diamonds used in grinding segments for stone and concrete machining. Mat.-wiss. u. Werkstofftech. 2016;47(12):1193–201. https://doi.org/10.1002/mawe.201600713.
[38] Tillmann W, Ferreira M, Steffen A, Rüster K, Möller J, Bieder S, et al. Carbon reactivity of binder metals in diamond–metal composites – characterization by scanning electron microscopy and X-ray diffraction. Diam Relat Mater 2013;38:118–23. https://doi.org/10.1016/j.diamond.2013.07.002.
[39] Tillmann W, Tolan M, Lopes-Dias NF, Zimpel M, Ferreira M, Paulus M. Influence of chromium as carbide forming doping element on the diamond retention in diamond tools. International Conference on Stone and Concrete Machining (ICSCM) 2015;3:21–30. https://doi.org/10.13154/icscm.3.2015.21-30 (2015).
[40] Tillmann W, Tolan M, Lopes-Dias NF, Zimpel M Ferreira M, Paulus M, editors. Influence of chromium as carbide forming doping element on the diamond retention in diamond tools; 2015.
[41] Yeh J-W. Alloy design strategies and future trends in high-entropy alloys. JOM 2013;65(12):1759–71. https://doi.org/10.1007/s11837-013-0761-6.
[42] Zhang Y, Lu ZP, Ma SG, Liaw PK, Tang Z, Cheng YQ, et al. Guidelines in predicting phase formation of high-entropy alloys. Mrs Communications 2014;4(2):57–62.
[43] Gao MC, Yeh J-W, Liaw PK, Zhang Y. High-entropy alloys. Cham: Springer International Publishing; 2016.
[44] Boer, Frank R de, Mattens WCM, Boom R, Miedema AR, Niessen AK. Cohesion in metals: transition metal alloys. Amsterdam: North-Holland; 1988.
[45] Kursun C, Gogebakan M. Characterization of nanostructured Mg–Cu–Ni powders prepared by mechanical alloying. J Alloys Compd 2015;619:138–44. https://doi.org/10.1016/j.jallcom.2014.08.126.
[46] Suryanarayana C. Mechanical alloying and milling. Prog Mater Sci 2001;46(1–2):1–184. https://doi.org/10.1016/S0079-6425(99)00010-9.
[47] Tillmann W, Ulitzka T, Wojarski L, Manka M, Ulitzka H, Wagstyl D. Development of high entropy alloys for brazing applications. Weld World 2020;64(1):201–8. https://doi.org/10.1007/s40194-019-00824-y.
[48] Chipman J. Thermodynamics and phase diagram of the Fe-C system. Metall Trans A 1972;3(1):55–64. https://doi.org/10.1007/BF02680585.
[49] Benz R, Elliott JF, Chipman J. Solid phases of the Mn-C system. Metall Trans A 1973;4(6):1449–52. https://doi.org/10.1007/BF02667992.